

## Target charging in short-pulse-laser–plasma experiments

J.-L. Dubois,<sup>1</sup> F. Lubrano-Lavaderci,<sup>1</sup> D. Raffestin,<sup>1</sup> J. Ribolzi,<sup>1</sup> J. Gazave,<sup>1</sup> A. Compant La Fontaine,<sup>2</sup> E. d’Humières,<sup>3</sup> S. Hulin,<sup>3</sup> Ph. Nicolai,<sup>3</sup> A. Poyé,<sup>3</sup> and V. T. Tikhonchuk<sup>3,\*</sup>

<sup>1</sup>CEA/DAM/CESTA, BP 12, Le Barp 33405, France

<sup>2</sup>CEA/DAM/DIF, F-91297 Arpajon, France

<sup>3</sup>Centre Lasers Intenses et Applications, University Bordeaux, CNRS, CEA, Talence 33405, France

(Received 2 October 2013; published 13 January 2014)

Interaction of high-intensity laser pulses with solid targets results in generation of large quantities of energetic electrons that are the origin of various effects such as intense x-ray emission, ion acceleration, and so on. Some of these electrons are escaping the target, leaving behind a significant positive electric charge and creating a strong electromagnetic pulse long after the end of the laser pulse. We propose here a detailed model of the target electric polarization induced by a short and intense laser pulse and an escaping electron bunch. A specially designed experiment provides direct measurements of the target polarization and the discharge current in the function of the laser energy, pulse duration, and target size. Large-scale numerical simulations describe the energetic electron generation and their emission from the target. The model, experiment, and numerical simulations demonstrate that the hot-electron ejection may continue long after the laser pulse ends, enhancing significantly the polarization charge.

DOI: [10.1103/PhysRevE.89.013102](https://doi.org/10.1103/PhysRevE.89.013102)

PACS number(s): 52.38.Kd, 41.75.Jv, 52.57.Kk

### I. INTRODUCTION

Interaction of high-energy and high-power laser pulses with solid targets is accompanied with the generation of a significant number of energetic electrons, producing many secondary effects. The intense x-ray emission [1], ion acceleration [2,3], and many other effects [4] have been intensively studied and have been used in many applications. However, there is a domain related to the laser electron acceleration, which has not been fully described yet. This is the generation of intense electromagnetic pulses during and after the laser pulse spanning a very broad frequency range from a fraction of a terahertz to a megahertz. No single physical mechanism can explain this phenomenon, which has long attracted the attention of many researchers. In particular, the low-frequency part of the emission spectra in the GHz range has been measured in many experimental facilities, especially in the case of multiterawatt laser pulses of a picosecond duration [5]. Such fields may exist in the experimental chamber for a time of the order of microseconds after the laser pulse and may be dangerous for the operation equipment and diagnostics. The mechanisms of generation of electric and magnetic fields in this frequency domain are not well known. It is accepted that the fields are generated during the interaction of the laser pulse with the target and increase with the ejected charge [6–8], but the exact mechanism is not yet defined. It could be related either to the electric current carried out by escaping electrons or with the charge accumulated on the target. The experimental data indicate that the signal strength and the temporal profile depend on the target material and geometry [9], on the shape and the place of the metallic elements of the chamber, as well as on the laser pulse intensity and duration. In particular, the electromagnetic pulses generated with intense picosecond pulses have a much higher amplitude than the

ones generated from nanosecond pulses of a much higher energy [10].

In this paper, we present the theoretical model describing the source of electromagnetic emission, which is the target polarization induced by the escaping energetic electrons created in the interaction of intense picosecond or subpicosecond laser pulses with solid targets. This model is verified in a specially designed experiment where the target return current is directly measured. The experimental data are compared with a series of numerical simulations describing the generation and emission of energetic electrons from the target. It is shown that the target charging proceeds long after the end of the laser pulse. The charged zone at the target surface expands with the hot-electron velocity, thus increasing the target capacity and facilitating the escaping of electrons. Thus, the target lateral size could have a significant impact on the overall polarization effect. The model of charge accumulation is presented in Sec. II for the case of intense picosecond laser pulses and massive targets. It predicts the target charge value in function of the effective energy of hot electrons generated by the laser pulse and the target characteristics. The theoretical predictions are verified in a specially designed experiment, where the accumulated charge has been measured in function of the target size and the laser pulse duration and energy. The experimental results are presented in Sec. III. The experimental data are modeled in a series of numerical simulations, which are discussed in Sec. IV. The three-dimensional particle-in-cell code describes the hot-electron production in the laser focal spot. The subsequent propagation of the energetic electrons and their ejection from the target is modeled with a Monte Carlo code. Finally, the propagation of the ejected electrons in the interaction chamber is described with an electromagnetic particle code. These multiscale extensive numerical simulations demonstrate a good agreement with the experimental data and confirm the basic model assumptions. The conclusions and the model predictions for several high-intensity laser installations are presented in Sec. V. A combination of the theoretical model, numerical simulations, and the experiment

\*tikhonchuk@celia.u-bordeaux1.fr

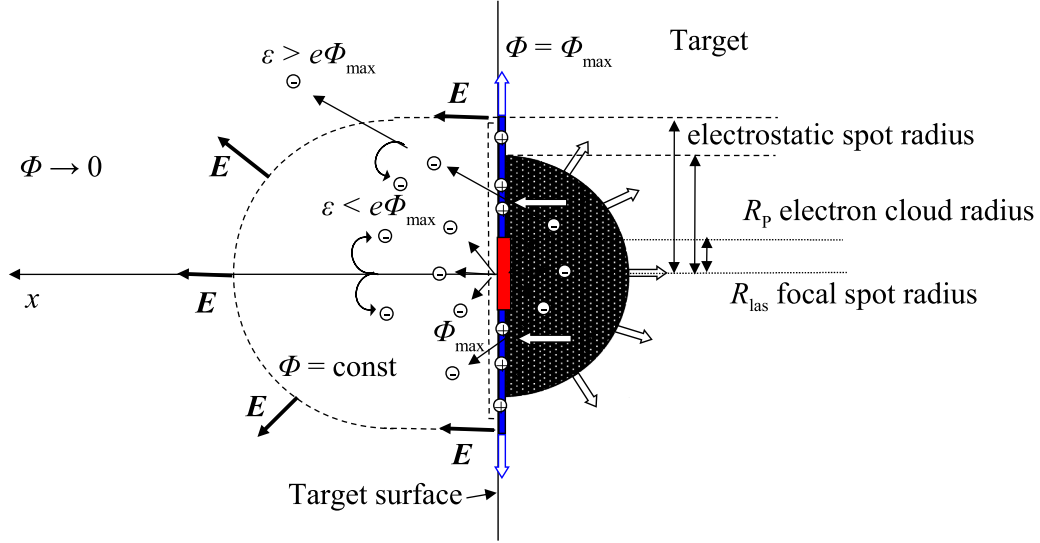


FIG. 1. (Color online) Scheme of the target charge and the electric field in the case of short-pulse interaction with a thick solid target. Hot electrons are created in the laser focal spot (red zone). They are spreading in the target over the distance comparable to the mean free path (gray zone). Some of the electrons are escaping in vacuum, creating a spatial charge and preventing the electrons with the energies smaller than the target potential from escaping. The electrons with the energies higher than the surface potential can escape from the target, thus creating a net positive charge at the surface.

provides a consistent explanation of target polarization and formation of the electromagnetic signal after the end of the laser pulse.

## II. A SIMPLIFIED MODEL OF CHARGE ACCUMULATION ON THE TARGET IN LASER-PLASMA INTERACTION

The energetic electrons ejected from the target are identified as the dominant source creating an electromagnetic radiation during and after the end of the laser pulse [6,7]. However, the exact mechanism of the electromagnetic pulse (EMP) generation is not yet identified. It could be related with the current associated with fast electrons escaping from the target [5] or with a discharge current to a positively charged target. It is thus important to understand the processes leading to the target polarization and to develop a model providing an estimate of the accumulated target charge. The scheme of the target charging is presented in Fig. 1 for the case where the target size is larger than the hot-electron mean free path.

For the laser pulses of a picosecond duration, one can neglect the charge neutralization by the electrons coming from the target support elements. Then the target charging process can be described by the following steps:

(i) The laser pulse deposits its energy at the target surface. It is partially converted into the hot electrons with the conversion efficiency  $\eta_{\text{abs}}$ .

(ii) The electrons accelerated in the backward direction are ejected from the target in vacuum, thus creating a potential drop  $\Phi$  in the Debye layer at the target surface. This potential confines the major part of escaping electrons and returns them back to the target.

(iii) The hot electrons accelerated in the forward direction expand outside the laser focal spot. The diffusion is dominated by the elastic collisions with ions. The collisions with the target

thermal (or bind) electrons define the hot-electron cooling time.

(iv) The deficit of the electrons in the laser spot is compensated with the return current of cold electrons, so the target remains electrically neutral.

(v) Some of scattered hot electrons are ejected from the target as long as their temperature remains sufficiently high. The most energetic electrons escape from the Debye layer, thus producing a net positive charge on the target. The cooling process defines the maximal time of the target charging.

The goal of this section is to develop a sufficiently simple quantitative model of the target charging that is capable of predicting the net residual charge and the charging time of a thick target irradiated by a short intense laser pulse. It will be shown that the target-charging process takes a few picoseconds. It is much shorter than the discharge current time, which is defined by the impedance of the whole target support ensemble. It is typically in the nanosecond time scale, as shown in Sec. III A.

### A. Distribution function of hot electrons

We assume in the model that the distribution function of hot electrons created in the laser focal spot at the target surface is described by an isotropic relativistic Maxwell-Jüttner function,

$$f_h(\varepsilon) = (n_h/4\pi A_h m_e^3 c^3) \exp(-\varepsilon/T_h),$$

depending on the electron energy  $\varepsilon = \sqrt{m_e^2 c^4 + p^2 c^2} - m_e c^2$ . Here  $p$  is the electron momentum,  $n_h$  is the hot-electron density,  $m_e$  is the electron mass,  $c$  is speed of light,

$$\begin{aligned} A_h(T_h) &= (m_e c)^{-3} \int dp p^2 \exp(-\varepsilon/T_h) \\ &= (T_h/m_e c^2) e^{m_e c^2/T_h} K_2(m_e c^2/T_h) \end{aligned}$$

is the normalization constant, and  $K_2$  is the modified Bessel function of the second kind. The function  $A_h$  varies as  $\sqrt{\pi/2}(T_h/m_e c^2)^{3/2}$  in the nonrelativistic limit,  $T_h \ll m_e c^2$ , and as  $2(T_h/m_e c^2)^3$  in the ultrarelativistic limit,  $T_h \gg m_e c^2$ .

The exponential hot-electron distribution in energy has been observed in many experiments and numerical simulations for laser intensities above  $10^{16}$ – $10^{17}$  W/cm<sup>2</sup>. The angular distribution of laser-created hot electrons could be anisotropic, but this is not the crucial element of the model. As we will demonstrate below, the electron ejection takes place in a time scale that is longer than the electron collision time in the target when the electrons are already isotropic.

The temperature of hot electrons  $T_h$  created by intense laser pulses on a surface of a solid target depends on many parameters, such as the laser polarization, the incident angle, and so on. However, the major parameter is the square of the dimensionless laser amplitude  $a_0$ , which is proportional to the product of the laser pulse intensity  $I_{\text{las}}$  and the square of the laser wavelength  $\lambda_{\text{las}}$ . This dependence has been evaluated in many experiments. As a rough estimate, it can be described either by the empirical Beg's law [11,12] if the laser intensity is below  $10^{18}$ – $10^{19}$  W/cm<sup>2</sup> or by the ponderomotive scaling for higher intensities. In the model we use the following interpolation:

$$T_{h0} \simeq m_e c^2 \max \left\{ 0.47 a_0^{2/3}, \sqrt{1 + a_0^2} - 1 \right\}, \quad (1)$$

where  $a_0 = 0.85 \times 10^{-9} \lambda_{\text{las}} I_{\text{las}}^{1/2}$ ,  $I_{\text{las}}$  is in W/cm<sup>2</sup>, and  $\lambda_{\text{las}}$  is in microns. In the domain of interest, for the laser intensities of the order of  $10^{17}$ – $10^{19}$  W/cm<sup>2</sup> the parameter  $a_0$  varies in the range from 0.3 to 3, and the electron temperature  $T_h$  from 0.1 to 1.1 MeV.

The total number of hot electrons  $N_{h0}$  can be related to the laser pulse energy by the energy conservation,

$$N_{h0} = \eta_{\text{abs}} \mathcal{E}_{\text{las}} / \langle \varepsilon_e \rangle, \quad (2)$$

where the parameter  $\eta_{\text{abs}}$  characterizes the laser energy absorption and

$$\begin{aligned} \langle \varepsilon_e \rangle &= \frac{4\pi}{n_h} \int dp p^2 \varepsilon f_h \\ &= m_e c^2 \left[ 3 \frac{T_h}{m_e c^2} + \frac{K_1(m_e c^2/T_h)}{K_2(m_e c^2/T_h)} - 1 \right] \end{aligned}$$

is the average hot-electron energy. The ratio of  $\langle \varepsilon_e \rangle$  to  $T_h$  is 3/2 in the nonrelativistic limit and it increases to 3 in the limit of ultrarelativistic temperatures.

The efficiency of laser energy conversion into hot electrons depends on the details of the acceleration process. A simple empirical scaling  $\eta_{\text{abs}} \propto I_{\text{las}}^{0.266}$  was proposed in Ref. [13] based on the interpolation of the results of experiments and numerical simulations. However, the proportionality coefficient strongly depends on particular experimental conditions, on the target material, and on the laser prepulse. For this reason, we consider below  $\eta_{\text{abs}}$  as an empirical parameter. According to the numerical simulations discussed in Sec. IV, the absorption efficiency is  $\sim 40\%$  in the Eclipse experiment discussed in the next section.

## B. Collisions of hot electrons

The hot electrons accelerated in the laser focal spot expand in the target. The collisions between hot electrons can be neglected, but they are scattered elastically in the collisions with target ions and lose their energy in the collisions with cold electrons. The electron stopping length depends on the electron energy and the target density [14]. The electron range  $R_s$  is defined as a distance where the electrons are losing a significant part of their energy. A convenient interpolation for the electron range  $R_s$  was proposed in Ref. [15] as follows:

$$\begin{aligned} \rho_t R_s &\simeq 0.276 A_t Z_t^{-8/9} \varepsilon_e^{5/3} (1 + 0.978 \varepsilon_e)^{5/3} \\ &\times (1 + 1.957 \varepsilon_e)^{-4/3} \text{ g/cm}^2, \end{aligned} \quad (3)$$

where the electron energy  $\varepsilon_e$  is in MeV,  $\rho_t$  is the target density,  $A_t$  the target atomic mass, and  $Z_t$  is the atomic number. This expression agrees very well with the experimental data for a broad range of target materials and for the electron energies up to a few MeV. The electron diffusion length due to the elastic scattering on ions can be expressed as  $R_{\text{dif}} = R_s/(1+g)$ , where the factor  $g = 0.187 Z_t^{2/3}$  [15] is the effective ratio of the electron-ion to electron-electron collision rates.

A significant part of the laser-accelerated electrons propagate inside the target. However, there is a finite probability that the electrons are scattered in a collision with ions at a large angle and are ejected from the target. The probability of electron backscattering  $r_B$  and the characteristic angle of ejection  $\theta_B$  are defined by the factor  $g$  as follows:

$$\begin{aligned} \tan \theta_B &= 2.2 g (1 + g) / (1 + 2g - 0.21 g^2), \\ r_B &= \sin^2(\theta_B/2). \end{aligned} \quad (4)$$

In particular, for a copper target used in our experiment,  $g = 1.76$ ,  $\theta_B = 70^\circ$ , and  $r_B = 0.33$ .

It is important to make a difference between the collision length (3) corresponding to a monoenergetic electron beam and the mean stopping length  $\langle R_s \rangle$  averaged over the electron distribution function,

$$\langle R_s \rangle = \frac{4\pi}{n_h} \int dp p^2 R_s(\varepsilon) f_h.$$

For the case of a Maxwellian electron distribution, the mean electron stopping length is approximately 4 times larger than the stopping length of an electron having the energy equal to the temperature.

## C. Temporal evolution of hot electrons

A generic laser pulse with a Gaussian temporal and spatial shape is approximated in the model with steplike distributions. The laser pulse is assumed to have the same energy at a constant intensity  $I_{\text{las}}$  over the time  $t_{\text{las}}$  and over the circular spot of a radius  $R_{\text{las}}$ . Moreover, we consider the following simplified model for the temporal evolution of the hot-electron density and temperature. The total number of electrons in the cloud  $N_h$  increases linearly during the laser pulse and remains constant after that, while the hot-electron temperature

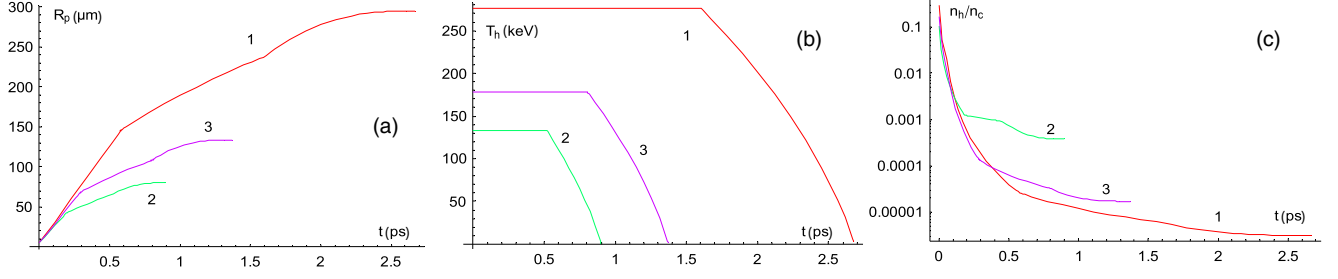


FIG. 2. (Color online) Temporal dependence of the radius of the hot-electron cloud  $R_p$  (a), the hot-electron temperature  $T_h$  (b), and the density,  $n_h/n_c$ , (c) for the cases corresponding to the Eclipse laser experiment: the laser spot diameter  $D_{\text{las}} = 7.5 \mu\text{m}$ ,  $\lambda_{\text{las}} = 0.8 \mu\text{m}$ , a copper target; red lines (1):  $\mathcal{E}_{\text{las}} = 0.1 \text{ J}$ ,  $t_{\text{las}} = 50 \text{ fs}$ ; green lines (2):  $\mathcal{E}_{\text{las}} = 0.1 \text{ J}$ ,  $t_{\text{las}} = 400 \text{ fs}$ ; violet lines (3):  $\mathcal{E}_{\text{las}} = 0.03 \text{ J}$ ,  $t_{\text{las}} = 50 \text{ fs}$ . The laser energy absorption is 40% in all cases.

$T_h$  remains approximately constant during the laser pulse, while it decreases after that. These assumptions are not too restrictive as we are interested in the total number of ejected electrons but not their temporal evolution.

The temperature and density evolution are defined by the time dependence of the radius of electron cloud  $R_p$ . The electron diffusion length  $\langle R_{\text{dif}} \rangle = \langle R_s \rangle / (1 + g)$  was introduced in the previous subsection. The temporal evolution of the electron cloud radius can be described by the diffusion equation,

$$dR_p^2/dt = \langle R_{\text{dif}} \rangle v_h, \quad (5)$$

with the average electron velocity,  $v_h$ , defined as follows:

$$v_h = \frac{4\pi}{n_h} \int dp p^2 v f_h = \frac{2 T_h^2}{m_e^2 c^3 A_h} \left( 1 + \frac{T_h}{m_e c^2} \right).$$

The diffusion model for the electron cloud applies after at least one electron-ion collision time. So we assume that for the times shorter than  $t_{ei} = \langle R_{\text{dif}} \rangle / v_h$  the electrons are expanding freely with the velocity  $v_h$ , and Eq. (5) applies for  $t > t_{ei}$  with the initial condition  $R_p(t = t_{ei}) = R_{\text{las}} + \langle R_{\text{dif}} \rangle$ . Therefore the time dependence of the characteristic radius of electron cloud reads

$$R_p(t) = \begin{cases} R_{\text{las}} + v_h t & \text{if } 0 < t < t_{ei}, \\ \sqrt{(R_{\text{las}} + v_h t_{ei})^2 + \langle R_{\text{dif}} \rangle v_h (t - t_{ei})} & \text{if } t_{ei} < t < t_{\text{cool}} + t_{ei}. \end{cases} \quad (6)$$

These expressions are valid as long as the electron temperature remains constant. The electron cooling is due to the electron-electron collisions. The corresponding time can be estimated as  $t_{ee} = \langle R_s \rangle / v_h = t_{ei}(1 + g)$ . Then the equation for the electron temperature evolution for  $t > t_{ee}$  reads

$$dT_h/dt = -T_h/t_{ee}. \quad (7)$$

In the collisional model proposed in Ref. [15], see Sec. II B, the electron stopping power depends on the electron temperature in the power 5/3 in the nonrelativistic limit. Correspondingly,  $t_{ee} \propto T_h^{7/6}$  and the electron temperature decreases with time as  $(1 - t/t_{\text{cool}})^{6/7}$ , where  $t_{\text{cool}} = (6/7)t_{ee}$  with  $t_{ee}$  evaluated at the initial hot-electron temperature. In the strongly relativistic case the electron stopping power is proportional to the square of temperature and, correspondingly, the electron temperature decreases with time as  $(1 - t/t_{\text{cool}})^{1/2}$  where  $t_{\text{cool}} = (3/5)t_{ee}$ . In the model, we integrated Eqs. (5) and (7) for  $t > t_{ei}(1 + g)$  numerically and defined  $t_{\text{cool}}$  as the time where the electron temperature drops by a factor of 100 from its initial value.

The volume of the electron cloud can be represented as a cylinder of radius  $R_p$  and the height  $x_p = R_p - R_{\text{las}}$ . The total hot-electron number increases linearly during the laser pulse, and then it stays constant. Correspondingly, the time

dependence of the hot-electron density can be described as follows:

$$n_h = \frac{N_{h0}}{\pi R_p^2 (R_p - R_{\text{las}})} \begin{cases} t/t_{\text{las}} & \text{if } 0 < t < t_{\text{las}}, \\ 1 & \text{if } t_{\text{las}} < t. \end{cases} \quad (8)$$

Examples of temporal evolution of the hot-electron temperature, density, and the radius of the hot-electron cloud are shown in Fig. 2 for the parameters of the experiment discussed in the next section. The electron cooling time in this case varies from 0.5 to 1 ps, so the hot electrons stay in the target a long time after the end of the laser pulse. The radius of electron cloud increases almost linearly with time attaining the values from 80 to 300  $\mu\text{m}$ . These distances are compatible with the experimental observations [16] and the numerical simulations [17], showing a fast spreading of hot electrons and the corresponding  $K\alpha$  emission from the target. The hot-electron density is of the order of the critical density  $n_c = 1.1 \times 10^{21} / \lambda_{\text{las}}^2 \text{ cm}^{-3}$  during the laser pulse. However, it decreases dramatically by 3–5 orders of magnitude during the time of hot-electron expansion and cooling.

The assumption of a homogeneous electron density and temperature within the cloud is certainly rather crude, but it is justified by the simplicity of the model and the comparison presented in Sec. IV B, with the results detailed in numerical

simulations, which are in good agreement with the model predictions.

#### D. Electric potential of the charged zone

The electric potential  $\Phi$  at the target surface is created by the electrons that are escaping from the target but repelled back by the space charge. In the simplest case of a monoenergetic electron distribution,  $f_h \propto \delta(\varepsilon - \varepsilon_0)$ , the potential jump is equal to  $\varepsilon_0/e$  and the electrons are stopped at the distance  $\sim(\varepsilon_0\varepsilon_0/e^2n_h)^{1/2}$ , where  $\varepsilon_0$  is the vacuum dielectric permittivity and  $e$  is the elementary charge. Thus escaping electrons create a virtual cathode. No electrons escape from this layer.

In the case of a Maxwellian electron energy distribution the characteristic thickness of the sheath layer is defined by the Debye length of hot electrons  $\lambda_{Dh} \simeq (\varepsilon_0 T_h / e^2 n_h)^{1/2}$ . According to the one-dimensional model [18–20] recalled in the appendix, the electron density decreases inversely proportional to the square of the distance from the target, Eq. (A4), and the electrostatic potential decreases logarithmically  $e\Phi(x) \simeq -2T_h \ln(\sqrt{e} + x/\lambda_{Dh}\sqrt{2})$ . This expression is valid for a steep target density profile with the characteristic scale smaller than  $\lambda_{Dh}$ . It may not be appropriate for pulses with a low contrast or of a duration longer than a few ps.

The potential jump is limited in a more realistic case where the hot electrons are distributed within a disk of a radius  $R_p$ . Then the potential is limited at a distance  $x_{\max} \sim R_p$ , and the minimum potential can be estimated as  $e\Phi_{\min} \simeq -2T_h \ln(x_{\max}/\lambda_{Dh}\sqrt{2})$ . In order to account for a possible difference between  $x_{\max}$  and  $R_p$  in our simplified model, we defined the minimum potential as  $e\Phi_{\min} = -2T_h \ln(c_0 R_p / \lambda_{Dh}\sqrt{2})$  with the fitting coefficient  $c_0 = 1.0$ , which we chose from the comparison of the model with the numerical simulations and the experiment.

The knowledge of the electrostatic potential and the hot-electron parameters allows us to calculate the current of escaping electrons.

#### E. Ejection of hot electrons

The electrons with the energies  $\varepsilon > -e\Phi_{\min}$  escape from the target, leaving behind a net positive charge,  $Q$ . The current density of escaping electrons,  $j_h$ , can be written as

$$\begin{aligned} j_h &= -e \int d\Omega d\varepsilon p^2 \cos\theta f_h \\ &= -\frac{en_h \sin^2\theta_B}{4A_h(m_e c)^3} \int_{-e\Phi_{\min}}^{\infty} p^2 d\varepsilon e^{-\varepsilon/T_h}, \end{aligned} \quad (9)$$

where  $\theta$  is the polar angle with respect to the normal to target surface. The integral over the solid angle is taken over the angles of the electron ejection,  $\theta < \theta_B$ . The integral over the energies is taken over  $\varepsilon > -e\Phi_{\min}$ , corresponding to the escaping electrons. We assume that the potential  $\Phi_{\min}$  is homogeneous within the radius  $R_p$ , and it increases linearly to zero in the ring of the thickness of  $2\lambda_{Dh}$ .

Performing the integration over the electron energies and over the radius of the electron cloud in Eq. (9), we find the total polarization current  $J$ . It can be written as

follows:

$$\begin{aligned} J_h &= \frac{e\pi R_p^2 n_h c \sin^2\theta_B}{2A_h(T_h)} \left(\frac{T_h}{m_e c^2}\right)^2 \\ &\times \left[ \left[ \left(1 + \frac{e|\Phi_{\min}|}{T_h}\right) \left(1 + \frac{T_h}{m_e c^2}\right) + \frac{e^2\Phi_{\min}^2}{2T_h m_e c^2} \right] \right. \\ &\left. \times e^{-e|\Phi_{\min}|/T_h} + \frac{4\lambda_{Dh}T_h}{e|\Phi_{\min}|R_p} \left(1 + \frac{T_h}{m_e c^2}\right) \right]. \end{aligned} \quad (10)$$

This is the basic expression in our model. It provides the value of instantaneous current of escaping electrons. By integrating it over the time we calculate the charge accumulated on the target  $Q = \int J_h dt$ .

The expression (10) can be further simplified while neglecting the contribution from the Debye edge. In that case, the potential jump logarithmically depends on the size of the electron cloud and the approximate expression for the current reads

$$\begin{aligned} J &\simeq \frac{ec \sin^2\theta_B}{4c_0^2 r_e A_h(T_h)} \left(\frac{T_h}{m_e c^2}\right)^3 \left[ \left(1 + 2 \ln \frac{c_0 R_p}{\lambda_{Dh}\sqrt{2}}\right) \left(1 + \frac{T_h}{m_e c^2}\right) \right. \\ &\left. + \frac{2T_h}{m_e c^2} \ln^2 \frac{c_0 R_p}{\lambda_{Dh}\sqrt{2}} \right], \end{aligned} \quad (11)$$

where  $r_e = e^2/4\pi\varepsilon_0 m_e c^2$  is the electron classical radius. It is important to note that the escaping charge depends essentially on the hot-electron temperature and on the electron cooling time. In contrast, the dependence on the density of hot electrons is much weaker. The charge depends logarithmically on the hot-electron density and the radius of the electron cloud. In particular, in the case of nonrelativistic electron temperatures  $T_h \lesssim m_e c^2$ , the logarithmic term in the square brackets is of the order of 3–4. Therefore, the charging current depends essentially on the hot-electron temperature. According to Beg's law (1), it depends on the laser intensity in the power 1/3. Consequently, the charging current in the weakly relativistic case is approximately proportional to the square root of the laser intensity. It is linearly proportional to  $T_{h0}$ , and thus proportional to the square root of laser intensity in the strongly relativistic limit, where the ponderomotive scaling applies.

The charging current is approximately constant during the laser pulse and then it gradually decreases as the hot electrons cool down. The charging time is effectively the sum of the laser pulse duration and the electron cooling time, the latter being of the order of a few picoseconds. The charging time is effectively defined by the pulse duration for the case of ps laser pulses, and it is defined by the cooling time for the fs pulses. These dependencies are illustrated in Fig. 3 for the parameters of the experiment on the Eclipse laser presented in Sec. III.

Figure 3(a) shows the evolution of the potential jump in the Debye sheath. It decreases with time because of electron cooling and expansion. However, it remains all times higher than the hot-electron temperature shown in Fig. 2(b). The current of the escaping electrons is in the range of a few kiloamperes in the conditions of this experiment. It decreases with time as the electron density decreases.

According to Fig. 3, the target charge accumulation time is defined by the laser pulse duration in the case of a long pulse,

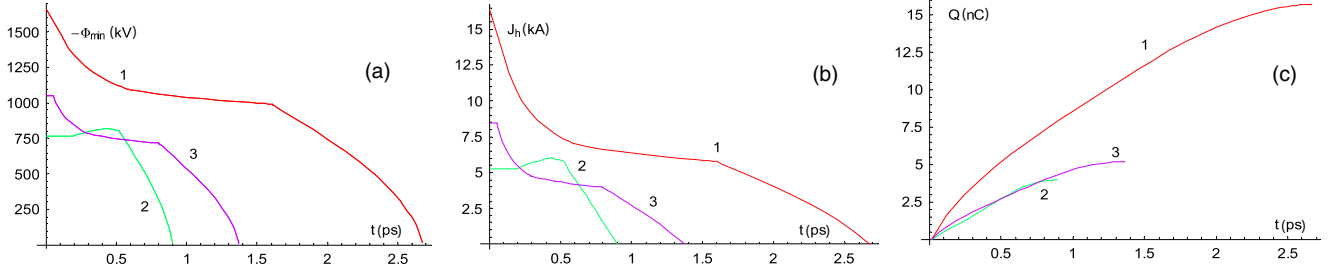


FIG. 3. (Color online) Temporal dependence of the potential drop in the Debye sheath  $\Phi_{\min}$  (a), the current of escaping electrons  $J_h$  (b), and the target net charge  $Q$  (c) for the cases corresponding to the Eclipse laser experiment:  $D_{\text{las}} = 7.5 \mu\text{m}$ ,  $\lambda_{\text{las}} = 0.8 \mu\text{m}$ , a copper target; red lines (1):  $\mathcal{E}_{\text{las}} = 0.1 \text{ J}$ ,  $t_{\text{las}} = 50 \text{ fs}$ ; green lines (2):  $\mathcal{E}_{\text{las}} = 0.1 \text{ J}$ ,  $t_{\text{las}} = 400 \text{ fs}$ ; violet lines (3):  $\mathcal{E}_{\text{las}} = 0.03 \text{ J}$ ,  $t_{\text{las}} = 50 \text{ fs}$ . The laser energy absorption is 40% in all cases.

and it is defined by the electron cooling time in the case of short pulses. The target charge increases approximately linearly with the laser pulse energy for a constant pulse duration, while it gradually decreases if the laser pulse duration increases for a constant pulse energy. A weaker dependence on the laser pulse duration is explained by a more intense charging current in the case of a longer laser pulse as the electron cooling is postponed [see Fig. 3(b)]. The charge of escaped electrons is of the order of a few nC, which corresponds to  $\sim 10\%$  of the total number of hot electrons generated in a laser target interaction.

One should make a difference among the total charge of hot electrons,  $Q_{\text{tot}} = eN_{h0}$ , the net charge of escaping electrons,  $Q$ , and the electric charge of electrons trapped in the sheath layer,  $Q_{\text{tr}}$ . The latter creates the potential barrier, which is higher than the average electron energy, since  $R_p \gg \lambda_{Dh}$ . Therefore, the major part of the electrons is stopped there and only a small number of suprathermal electrons may escape. Thus, we suppose in our model that  $Q \ll Q_{\text{tot}}$ . The escaping electrons do not affect the value of  $\Phi_{\min}$  too much, and the detailed structure of the potential barrier is not important for the calculation of the polarization current. The trapped charge can be estimated as  $Q_{\text{tr}} \simeq \pi R_p^2 \sigma_s$ , where the surface charge  $\sigma_s = \epsilon_0 E_s$  is related to the surface electric field  $E_s = -d\Phi/dx = \sqrt{2/e} T_h / e\lambda_{Dh}$ .

It is instructive to compare the net accumulated charge with the space charge in the sheath layer. For example, in the case of a short laser pulse presented with red lines in Fig. 3, the Debye length increases from a few microns during the laser pulse to about  $90 \mu\text{m}$  at the time when electron temperature decreases. The electric field at the target surface decreases rapidly from  $\sim 500 \text{ kV}/\mu\text{m}$  to about  $2 \text{ kV}/\mu\text{m}$  at the cooling time. The corresponding surface charge density  $\sigma_s = \epsilon_0 E_s$  decreases also by two orders of magnitude. However, the total charge in the Debye sheath increases up to  $\sim 10 \text{ nC}$  at the time of 1.5 ps and then it decreases again as the electrons are cooling down. It is comparable with the net target charge of 15 nC, but it is much smaller than the total charge of hot electrons, which is of the order of 70 nC.

The charging process is slowed down in the materials with a higher electron stopping power. For example, for the same conditions, the charge on a copper target is approximately 2 times smaller than that on an aluminum one. The present model describes massive targets, but it can be readily extended to thin foils by taking into account the recirculation effect similarly to Ref. [21].

### III. TARGET POLARIZATION EXPERIMENT

#### A. Experimental setup

The present model is compared with a dedicated experiment on the Eclipse laser system available at CELIA. It delivers a maximum of 100 mJ on target for a pulse duration as short as 50 fs at the wavelength of 800 nm. The temporal contrast measured by a third-order autocorellator is  $10^{-7}$  during the 2 ns preceding the main pulse. A  $f_{\#} = 5$  off-axis parabola is used to focus a linearly polarized laser beam at normal incidence on a target. The resulting focal spot presents a Gaussian shape profile of  $7.5 \mu\text{m}$  full width at half maximum (FWHM), as can be seen in Fig. 4(a). The high stability of a 10-Hz repetition rate laser system [shot to shot fluctuations are 2% root mean square (rms) in energy and 2% rms in duration] allows us to measure the target charge with good accuracy. In the results presented below each data point is averaged over five laser shots.

The model presented in Sec. II is valid for thick targets where the target thickness  $d$  is much larger than the range  $R_s$ , Eq. (3), of electrons in the material:  $d \gg R_s$ . For this reason we used  $d = 3 \text{ mm}$  thick copper targets, which is much larger than the 1-mm range corresponding to 1-MeV electrons in a solid copper. We have reproduced the experiment for three disk targets with diameters of 5, 10, and 15 mm. Each target was connected to the inner conductor of a coaxial cable by a straight brass wire of 0.5 mm radius. The distance between the copper disk center and the target holder plate, where the coaxial cable was fixed, was 5 cm whatever the target diameter. The target holder plate itself was connected to the ground but insulated from the coaxial cable.

This experimental setup is presented in Fig. 4(b). After each shot, electrons escaping from the target are propagating freely in vacuum up to the metallic experimental chamber walls 50 cm away. After the electron cooling the target exhibits a positive charge equal to the charge of escaped electrons. The specific design of the target holder allows us to measure the neutralization current of the target by connecting the coaxial cable to a Lecroy Wavemaster 8620A oscilloscope of 6-GHz bandwidth. To protect the oscilloscope from a high voltage, an attenuation of 60 dB was used. A typical form of the discharge current is presented in Fig. 5(a). The transfer function of the cable and the flange set was characterized after the experiment. The modulus of the attenuation function is displayed in Fig. 5(b). This attenuation was used to

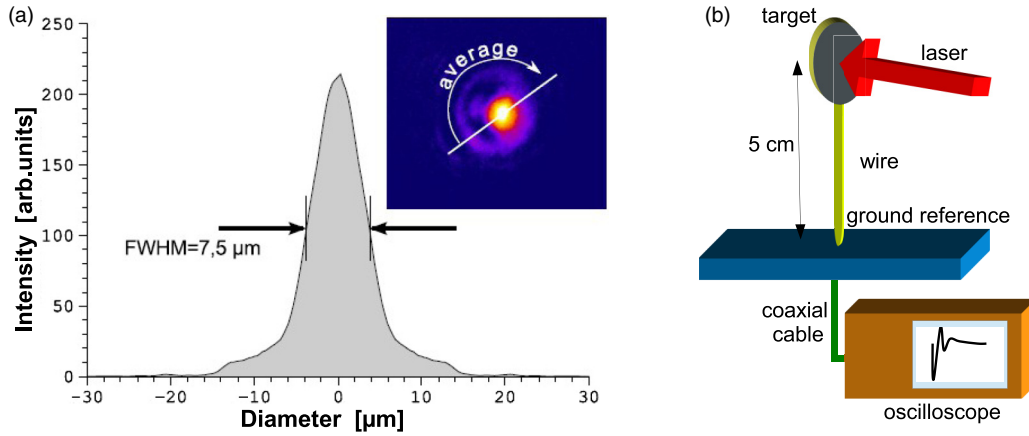


FIG. 4. (Color online) (a) Averaged laser focal spot lineout from the focal spot image (inset). (b) Scheme of the experimental setup.

correct the raw data. As the characteristic does not show any dispersion, no phase correction was applied. To account for the oscilloscope response, the following transfer function was used:

$$a_{\text{scope}}(\nu) = a_{\text{signal}}(\nu)(1 + i\nu/\nu_{\text{cut}})^{-1}, \quad (12)$$

where  $\nu_{\text{cut}} = 6 \text{ GHz}$  is the cutoff frequency.

**B. Experimental results**

A typical form of discharge current is displayed in Fig. 5(a). It corresponds to a shot onto a 10-mm-diameter target with an incoming energy of 80 mJ and a 50-fs pulse duration. The red solid line shows the data after processing. There is a minor difference from the raw data shown in black dots. The current waveform consists of one strong bipolar pulse with an amplitude of 40–50 A and a period of 1 ns followed by a second pulse of a smaller amplitude. These two pulsations were rather reproducible with small fluctuations. In some shots, at the time of 2.7 ns after the laser pulse, an overshoot of an amplitude of a few amperes was observed, as can be seen in the inset of Fig. 5(a). Its origin could be related to a reflected electromagnetic signal. After the laser shot, the target acts as an antenna. It may receive the electromagnetic signal induced

by the current discharge and reflected from the chamber walls. The total charge was calculated by integration of the current over time. To avoid biasing the charge estimate, the current was integrated up to 2.7 ns, as represented by the red area in Fig. 5(a).

The dependence of the target charge was studied in function of three parameters: the target diameter, the laser pulse duration, and the laser pulse energy. The measured total charge and the maximum current amplitude are shown in Figs. 6 and 7. In the first scan, the laser pulse duration was set to 50 fs and the laser pulse energy was varied from 10 to 100 mJ. In the second scan, the laser energy was kept constant at 80 mJ on the target, whereas the duration was tuned in the range from 50 to 550 fs.

The experimental points can be interpolated with simple linear functions. The total charge increases with the laser energy, independently of the target size. In contrast, the maximum current increases linearly with the laser energy but decreases with the target diameter. It can be readily understood as the larger target has a larger electric capacity and thus a larger discharge time. It is important to notice that, according to our measurements, the charge and the maximum current depend essentially on the laser energy and much less on the laser intensity. According to Fig. 7, the total target charge

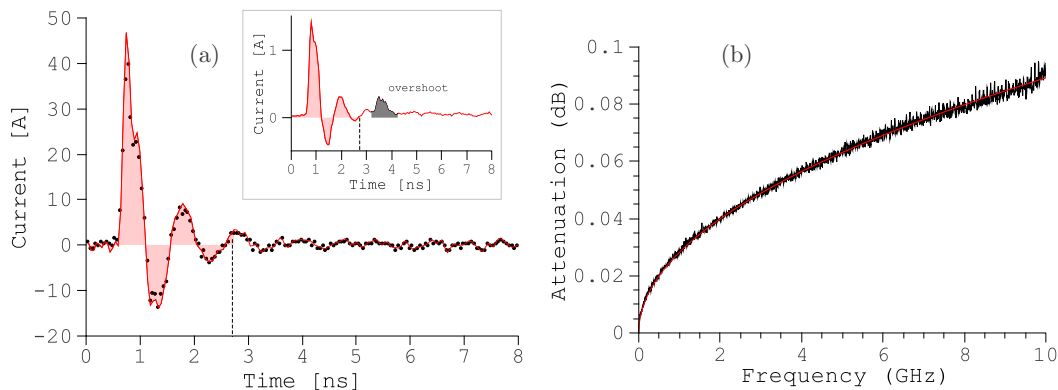


FIG. 5. (Color online) (a) Typical form of the discharge current (in A) as a function of time for 80 mJ on target laser pulse of a 50-fs duration. The points (·) are the raw data and the solid (red) line is the corrected signal. The shaded (orange) area represents the target charge obtained by integration of the current over time limited to 2.7 ns. (b) Attenuation function of the coaxial cable (in dB) in the frequency range from 0.1 to 10 GHz.

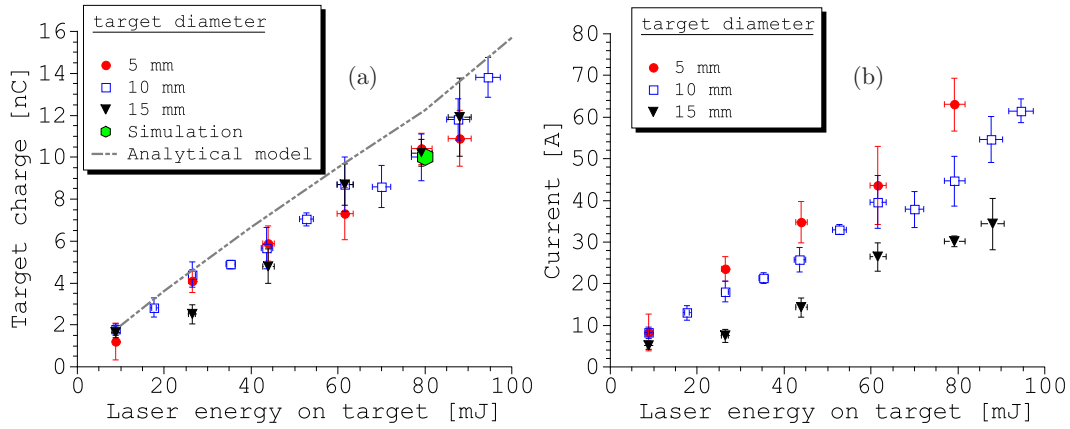


FIG. 6. (Color online) Dependence of the target charge [(a), in nC] and of the maximum current amplitude [(b), in A] as a function of the laser energy on target in the range from 10 to 100 mJ. The laser pulse duration is 50 fs and the target size is 5 mm (circles, red), 10 mm (open squares, blue), and 15 mm (triangles, black).

and the maximum current depend weakly on the laser pulse duration in the considered range from 50 to 550 fs.

According to the theoretical model presented in Sec. II, such behavior can be explained as follows. The scaling laws of Eq. (1) predict the hot temperature increase from 120 to 280 keV, while the laser energy increases from 10 to 100 mJ for the laser pulse duration of 50 fs. According to numerical solution of Eqs. (5), (7), and (10), the target charge increases from 2 nC at the minimum energy to approximately 15 nC at the maximum energy, which is in good agreement with the observations. The radius of the laser-heated zone  $R_p$  increases with time up to 300  $\mu\text{m}$  at the time  $\sim 2$  ps, which is much smaller than the minimum target size, see Fig. 2(a). Therefore, the independence on the polarization charge of the target size is in agreement with the theoretical model.

The model predicts the charging current amplitude up to 10–15 kA, which is much higher than the measured recharge current of 50 A maximum. This is also in agreement with the major hypothesis of the model, which neglects the recharging process. The characteristic recharging time of a few ns is

defined by the target size and the support assembly, which is a product of the capacity and the impedance of the electric circuit. The electric capacity of the copper disk is proportional to the disk size, while the wire impedance is a constant. This explains the decrease of the maximum current with the increase of the target size.

The second series of measurements of the charge dependence on pulse duration has been conducted at a constant laser pulse energy,  $\sim 0.1$  J. According to the analysis of Sec. II E, the number of ejected electrons depends on the ratio between the laser pulse duration and the hot-electron cooling time. These two quantities become equal for the pulse duration of about 0.4 ps. Correspondingly, for shorter pulse durations, the electron cooling time is longer and the ejected charge is larger. Oppositely, for a longer pulse duration the cooling time is short and the electrons are ejected essentially during the laser pulse. The ejected charge increases then with the laser pulse duration. Consequently, the ejected charge attains its minimum of  $\sim 7$  nC when  $t_{\text{las}} = 0.4$  ps. This non-monotonous behavior could be a reason for the observed very weak dependence of the ejected charge on the laser pulse duration.

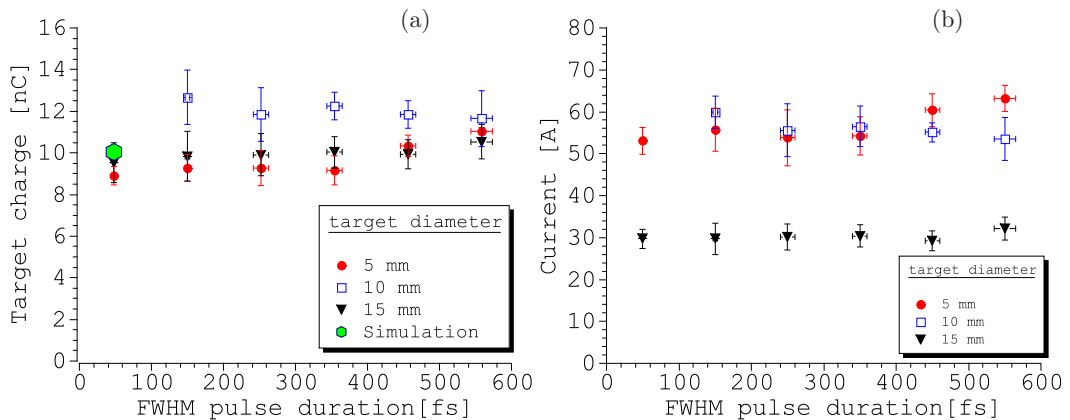


FIG. 7. (Color online) Dependence of the target charge [(a), in nC] and the maximum current amplitude [(b), in A] as a function of the laser pulse duration in the range from 50 to 500 fs. The laser pulse energy is 80 mJ and the target size is 5 mm (circles, red), 10 mm (open squares, blue), and 15 mm (triangles, black).

#### IV. NUMERICAL SIMULATIONS OF THE TARGET CHARGING

The Eclipse experiment was simulated with a suite of numerical codes that describe the dominant physical effects. As the real target size and the characteristic time are much larger than any code would accept, the simulation was conducted in four subsequent steps. First, the effect of laser prepulse on the solid target was simulated with the radiation hydrodynamic code CHIVAS [22,23]. It describes the plasma formation and its expansion from the solid target surface. Then the main laser pulse interaction with plasma and hot-electron generation were simulated in detail with the three-dimensional relativistic particle-in-cell (PIC) code CALDER [24,25]. These data were transferred in the Monte Carlo  $N$ -particle transport code (MCNP) [26] in order to model the propagation of hot electrons in the solid target and their collisions. Finally, the escape of electrons from the target and their propagation to the chamber elements was simulated with another PIC code, SOPHIE [27], that accounts for the target chamber geometry. Because of a large amount of required computing time, the simulations were conducted for a single set of parameters corresponding to the highest laser pulse energy and the shortest pulse duration.

##### A. Simulation of the electron source term

The prepulse of the laser Eclipse forms a preplasma that defines the interaction condition for the main laser pulse. The laser pulse arrives on the target at normal incidence. The preplasma conditions were computed with the one-dimensional radiative hydrodynamic code CHIVAS [22,23] assuming the laser prepulse intensity  $2 \times 10^{11}$  W/cm<sup>2</sup> (corresponding to the intensity contrast of  $10^7$ ) and a duration of 2 ns. The longitudinal plasma density profile along the axis  $x$  normal to the target at the moment of the main pulse arrival was approximated by an exponential function,  $n_e(x) = n_c \exp(-x/L_p)$ , with  $L_p = 3.4$   $\mu\text{m}$  and the position  $x = 0$  at the front target surface.

The main laser pulse interaction with the preplasma is modeled with the PIC code CALDER 3D [24,25] in a three-dimensional geometry. Hot electrons with energies up to a few MeV were produced by various physical processes that are described in the literature [28,29]. The most important among them is the ponderomotive or  $j \times B$  acceleration [30–33]. As the CALDER simulation box is much smaller than the hot-electron mean free path, the collisions of the laser accelerated electrons were accounted for separately at the subsequent simulation step.

The main laser pulse at the wavelength  $\lambda_{\text{las}} = 0.8$   $\mu\text{m}$  was linearly polarized along the  $y$  axis, with the energy at the target 80 mJ, the intensity at  $2 \times 10^{18}$  W/cm<sup>2</sup>, the peak normalized laser vector potential  $a_0 = 0.98$ , the spot size diameter at the half maximum of 8  $\mu\text{m}$ , and the pulse duration at the half maximum  $t_{\text{las}} = 50$  fs. In CALDER simulations, the temporal and radial laser profiles are assumed to be Gaussian functions. The simulations were run with a mesh size  $\Delta x = \Delta y = \Delta z = \lambda_{\text{las}}/30$ , 5 macroparticles per cell were used for electrons and 1 macroparticle per cell was used for ions. The CALDER simulation box dimensions were 30  $\mu\text{m}$  in the longitudinal ( $x$ ) direction and  $25 \times 25$   $\mu\text{m}^2$  in the transverse ( $y, z$ ) plane. The

laser pulse was injected from the left side of the simulation box. It propagates 4  $\mu\text{m}$  in the vacuum and then 21  $\mu\text{m}$  through the exponential density profile, increasing from 0.006 to 2.86  $n_c$ . The plasma density profile was terminated with a plateau of 5  $\mu\text{m}$  thickness at the density 2.86  $n_c$ .

During the simulation, the energy conservation was controlled by comparing the total kinetic energy gained by the plasma particles with the total Poynting flux integral. The difference was less than 3%. The boundary conditions for the fields are periodic at the transverse boundaries and absorbing at the longitudinal boundaries. For the particles, the boundaries are absorbing, provided that the total electric charge in the domain remains zero; otherwise particles are reinjected at the thermal velocity in order to keep the total charge equal to zero. CALDER simulations were performed with 600 processors during 50 h on the Tera100 Bull supercomputer at the CEA/DIF.

The characteristics of each macroparticle (position, velocity components, and weight) related to the accelerated electrons computed with CALDER were transferred in the Monte Carlo code MCNP 3D [26], which accounts for the collision processes of energetic electrons in the solid target in the three-dimensional geometry. They include the elastic collisions with the target electrons and ions and also the photon production in the Bremsstrahlung process. The latter process is not important here because of a very small photon conversion efficiency. About  $2 \times 10^9$  macroparticles were used. The simulation took about 17 h of the computing time on a standard monoprocessor workstation. The minimal energy considered in the CALDER and MCNP simulations was 50 keV in order to limit the computing time. The interaction was simulated during 500 fs, which is comparable but shorter than the electron cooling time shown in Fig. 2(b).

The scheme of the CALDER-MCNP 3D simulation is represented in Fig. 8(a). The electrons emitted from the CALDER simulation box forward and backward with respect to the laser direction were considered separately. Those emitted backward from the surface S1 (red arrays) do not interact with the target, while those emitted in the forward direction (blue arrays) interact with the solid target. The collision processes that take place in the target were computed with the MCNP code. The characteristics of electrons emitted from the backside of the target (surface S3) and the front side of the target (surface S2) calculated with the MCNP are discussed below. They present the output of this CALDER-MCNP simulation. The electron source term thus consists of the combined contributions of the electrons emitted and computed with CALDER (surface S1) and with MCNP (surfaces S2 and S3).

During the interaction of the main laser pulse with the short preplasma, 58% of the laser energy was reflected from the target. The preplasma thickness increases with time as the laser pulse propagates through. Thus, the reflected pulse interacts with a longer plasma and produces more energetic electrons (with the energies up to  $\sim 9$  MeV) in the backward direction compared to the forward accelerated electrons (the energy cutoff of  $\sim 3.5$  MeV) [24]. This can be seen in Fig. 8(b), where the distribution function of the electrons emitted from the CALDER box is presented in the polar coordinates  $(p_x, p_\perp)$ . As the laser pulse is weakly relativistic, the number of these relativistic electrons with the energies above 3.5 MeV

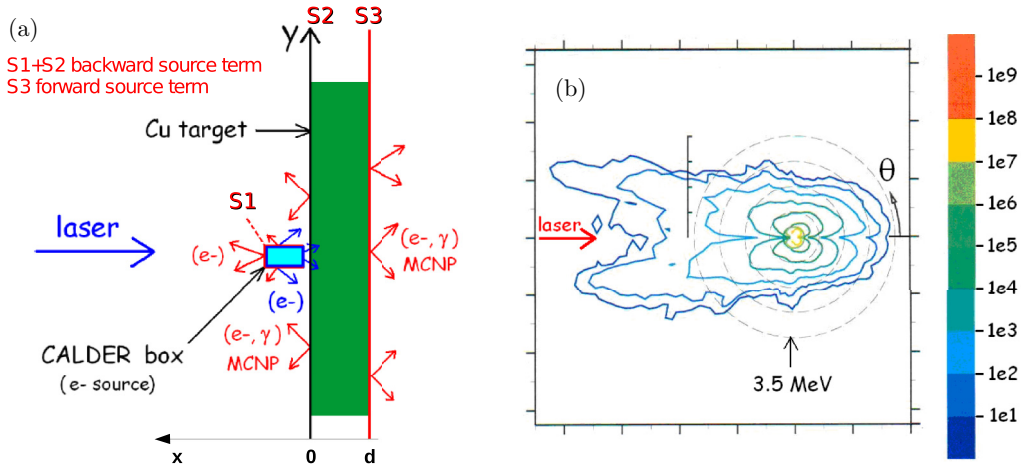


FIG. 8. (Color online) (a) Scheme of the coupling between the CALDER and MCNP codes in the  $(x, y)$  plane. The simulations were carried out in three dimensions. The laser enters from the left side of the CALDER simulation box (small box, blue). One part of the electrons exiting this box was emitted backward (small arrays, red) and the other part was emitted forward (blue arrays) and entered the copper target (large box, green). The collision processes taking place in copper were computed with MCNP. The electron emission was evaluated at the surfaces S1, S2, and S3. The emitted backward electrons at S1 were computed by CALDER, and the electrons emitted from the surfaces S2 and S3 backward and forward, respectively, were simulated by MCNP. (b) Energy distribution function in the polar coordinates of the electrons exiting the CALDER simulation box.

is relatively small,  $\sim 10^9$ , and they contribute less than 1% to the total target charge. The electron energy distribution is approximately exponential with the effective temperature  $T_{h0} \simeq 250$  keV. This value is in agreement with Eq. (1), that is, taking the maximum of the ponderomotive potential and the Beg's scaling. In total,  $5 \times 10^{11}$  electrons with energy greater than 50 keV were emitted from the CALDER simulation box. They carry out about 25% of the incident laser pulse energy. About 75% of these electrons were emitted in the forward direction with an angular aperture of the emission lobe of about  $83^\circ$ , while  $1.3 \times 10^{11}$  electrons are emitted backward (surface S1). These numbers are comparable with the total number of hot electrons,  $N_h = 4.2 \times 10^{11}$ , calculated from Eq. (2). The CALDER simulation box is smaller than the cutoff distance of the electrostatic potential. Thus, a significant part of electrons ejected from the CALDER box is not really free. Their evolution was studied in larger-scale simulations with the MCNP and SOPHIE codes.

The MCNP calculations indicate that only a small fraction  $2 \times 10^{-6}$  of the incident electrons are transmitted through the

target. This fraction corresponds to the mean ionization range of 0.2 mm for the electrons of the energy of 400 keV in a 3-mm layer of copper. There are about  $1.5 \times 10^{11}$  backscattered electrons ejected from the surface S2, which represents about 40% of the incident electrons. This number is in good agreement with the value of 33% given by the model estimate, Eq. (4). The energy distribution function of the electrons ejected backward from the surfaces S1 and S2 is represented in Fig. 9(a) for several angles with respect to the laser axis. The angular anisotropy is observed for electron energies exceeding 2–3 times the temperature. The characteristic opening angle of ejected electrons is in agreement with the theoretical description in Sec. II B.

The temporal dependence of the emitted backward electron current density is presented in Fig. 10. The backscattering process that takes place in the target tends to increase slightly the electron emission time to about 2 ps. In later time the electron emission continues from a larger target surface, but the total current is negligibly small. In total, about  $2.8 \times 10^{11}$  electrons left the simulation domain from the surfaces S1,

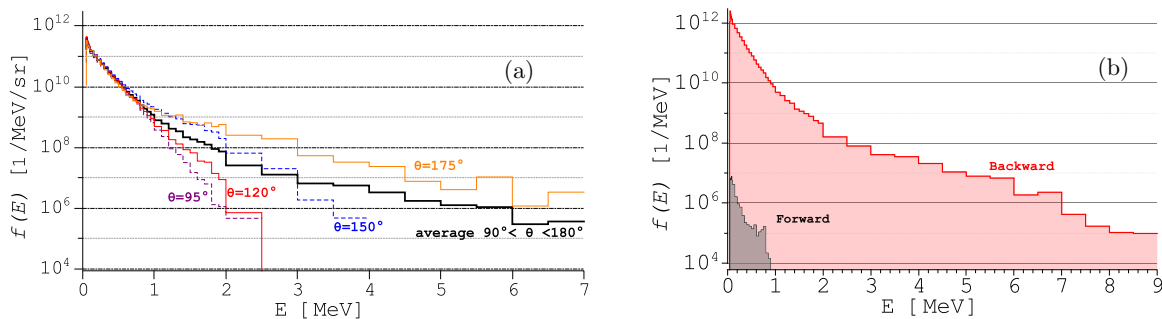


FIG. 9. (Color online) (a) Energy distribution function of electrons produced backwards (surfaces S1 and S2) at different angles, with respect to the laser axis. (b) Comparison of the energy distribution functions of the electrons emitted forward (surface S3) and backward (surfaces S1 and S2) from the MCNP and CALDER simulation boxes.

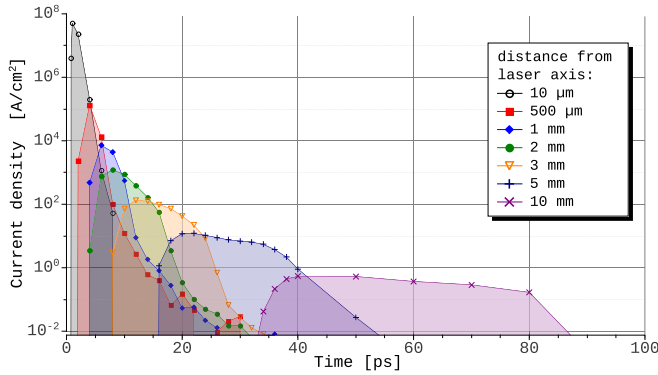


FIG. 10. (Color online) Time dependence of the current density of electrons emitted backwards (surface S2) at different distances from the laser axis obtained in the MCNP simulation.

S2, and S3. That represents a charge of 44 nC. The energy distribution of electrons transmitted in the forward direction (surface S3) and ejected backward from the surfaces S1 and S2 is presented in Fig. 9(b). The Bremsstrahlung emission is relatively small in this case. It produces an on-axis dose of about 1.8 μrad (or 18 nGy) at the distance of 1 m in air.

This numerical simulation in the MCNP code gives a 4 times bigger ejected charge than predicted by the model presented in Sec. II. According to Fig. 3(b), for the laser pulse energy of 0.1 J, at a time of 0.5 ps, the current is about 7.5 kA, the electron cloud radius is 120 μm, and the current density is about  $2 \times 10^7$  A/cm<sup>2</sup>. This is of the same order as shown in Fig. 10, although the current is more peaked in the simulation as the hot-electron density is inhomogeneous in the expanding cloud. However, the net target charge calculated in the model and with the code are of the same order.

**B. Simulation of the escaping charge**

The electric fields created by escaping electrons are not accounted for in the MCNP code. The simulations of CALDER and MCNP alone are not sufficient for a correct estimate of the electron charge escaped from the target. The large electrostatic

fields, produced on the target surface by the escaping electrons, were taken into account with the three-dimensional code SOPHIE [27]. It is specially designed for calculation of the system generated electromagnetic pulse (SGEMP) in laser-target interactions. This is a PIC finite difference in time domain (FDTD) code that solves the Maxwell’s equations for the fields and the Vlasov’s equations for the particles in vacuum in a volume limited by conducting or dielectric walls. The code works with billions of macroparticles tracked on billions of grid points with a prescribed boundary conditions.

The spectral, angular, temporal, and radial distribution of electrons leaving the solid target in the CALDER-MCNP boxes was taken as the input into the SOPHIE code. Only the electrons emitted in the backward direction are considered due to the very small fraction of transmitted electrons ( $2 \times 10^{-6}$ ). The target is assumed to be a perfect electrical conductor. The simulation domain was limited to a few millimeters around the target in order to perform a discretization with a micron-size grid. The absorbing conditions CPML [34] were imposed on the fields and the electrons at the external boundaries of the simulation volume. It has a cylindrical shape with a height of 2 mm and a radius of 2.5, 5, and 7.5 mm. The grid size was varied from 1 to 5 μm.

The profile of the electric potential distribution along the axis *x* perpendicular to the target surface is represented in Fig. 11(a). During the first picosecond, the potential increases, while the potential drop is localized at the target surface. The potential barrier forms after 1 ps, and it achieves the maximum of about 180 kV at the distance of 150 μm from the surface. The potential rising time of 2.5 ps is comparable with the characteristic duration of hot-electron emission (2 ps) and the time of crossing the simulation volume. The electron dynamics in the sheath layer explains the delay of the potential evolution compared to the model prediction shown in Fig. 3(a). Moreover, the comparison of the absolute value of the potential is not appropriate, because the model does not account for the sheath dynamics and the simulation does not account for the hot-electron distribution inside the target. Nevertheless, there is an agreement in the emission spot radius of 300 μm and the cooling time of 2.5 ps.

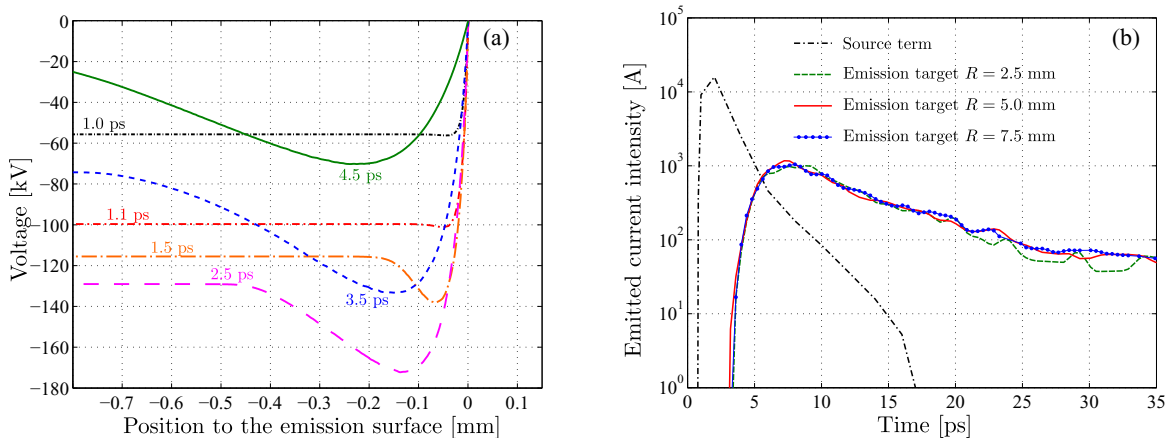


FIG. 11. (Color online) (a) Potential distribution at the front side of the target during the hot-electron emission at the time moments of 1, 1.1, 1.5, 2.5, 3.5, and 4.5 ps. The calculations with the code SOPHIE for the laser energy of 80 mJ and the pulse duration of 50 fs. (b) Time dependence of the electric current of escaping electrons collected at a distance of 1 mm from the target. Three simulations with the targets radii 2.5, 5, and 7.5 mm are shown. The dashed line shows the electric current extracted from the CALDER-MCNP boxes considered as a source term.

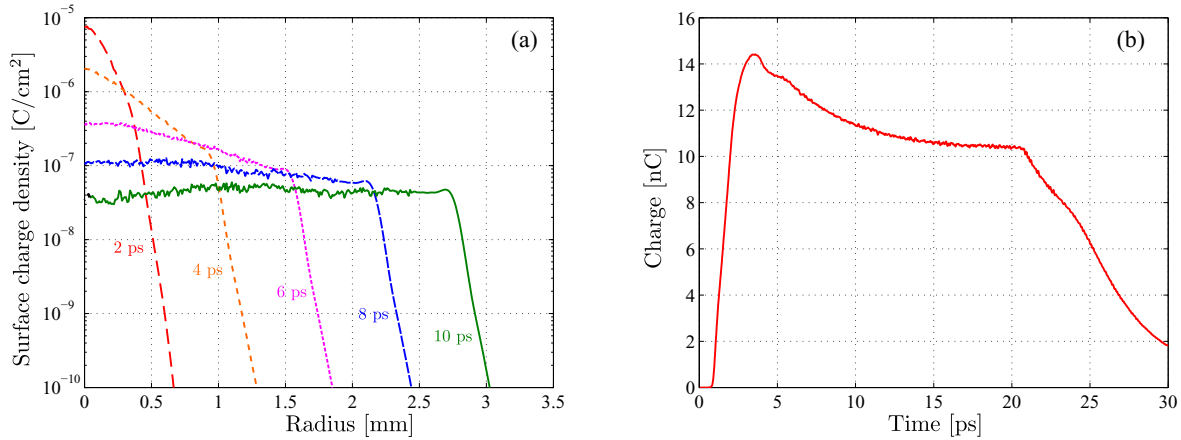


FIG. 12. (Color online) Surface charge density distribution over the front side of the target simulated with the SOPHIE code. The target radius is 5 mm, the pulse energy is 80 mJ, and the pulse duration is 50 fs. (b) Time dependence of the net surface charge obtained by integration of the surface charge density.

The electrons, which have escaped from the target, were collected at the boundary at the distance of 1 mm parallel to the target surface. This distance is sufficiently large for counting the electrons that have indeed escaped and will not be repelled back to the target. The electron current in function of time is presented in Fig. 11(b). Three simulations with the targets radii 2.5, 5, and 7.5 mm were performed with almost identical results. Thus, the escaped current does not depend on the size of the target for the considered conditions. This confirms the experimental observation that the accumulated charge does not depend on the target radius.

The potential at the target surface decreases with time after 4.5 ps because of the cooling of hot electrons. The delay of 3.5 ps is the time of propagation of the 1-mm distance from the target to the recording surface. The electron current achieves the maximum of about 1 kA at the time of 7 ps. The time delay of the maximum of electron emission of 3.5 ps is comparable with the electron cooling time of 1.5 ps in the model presented in Sec. II. As shown with the dashed curve in Fig. 11(b), almost all electrons are emitted in 2–3 ps.

The integration over the time gives an escaping charge of 10 nC. That represents one fourth of the emitted electrons, and it agrees rather well with the target charge measured in the experiment.

The current emission time of 7 ps is rather short to be affected by the boundary effect of the expansion of the positive charge over the target surface. As it is shown in Fig. 12(a), the radius of the positively charged zone increases with time almost linearly. The characteristic velocity is comparable with the hot-electron mean velocity. The essential charge is localized inside a radius of about 0.3 mm, corresponding to the emission surface defined by the electron range in the target, which is comparable with the electron cloud radius shown in Fig. 2(a) and with the mean hot-electron path  $\langle R_s \rangle \simeq 300 \mu\text{m}$  for the hot-electron temperature of 270 keV in a copper target. Thus, the accumulated charge should not depend on the target size for targets larger than 1 mm. That implies that the charge accumulated on targets with radius smaller than 0.5 mm could be less than the one calculated here. This charge builds up during the emission time of 3–5 ps [see Fig. 12(b)]. It rises to

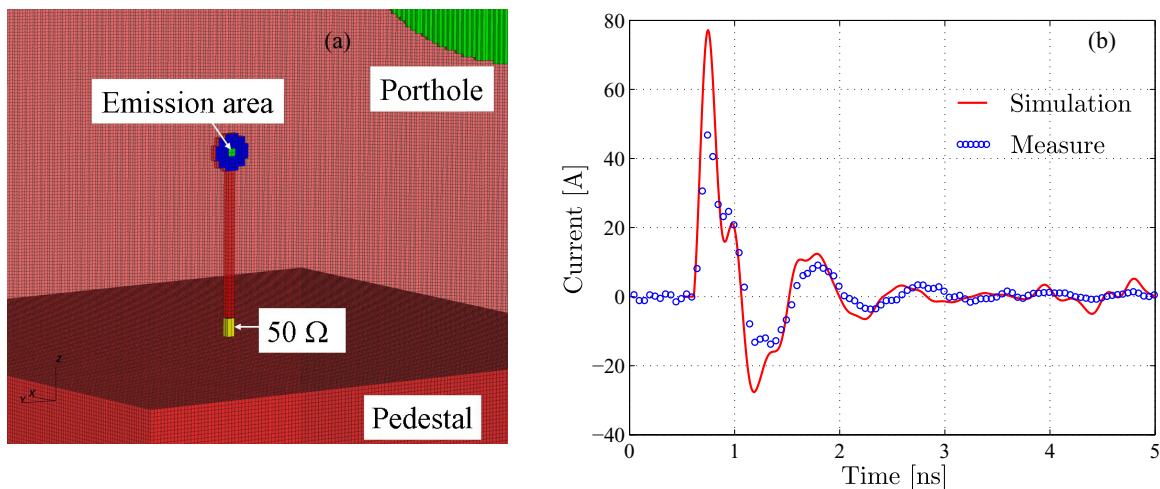


FIG. 13. (Color online) (a) Simulation of the current at the bottom of the target assembly in the Eclipse chamber. Calculation with the SOPHIE code: the target radius is 5 mm, the laser pulse energy 80 mJ, and the pulse duration 50 fs. The current is collected at an effective 50- $\Omega$  resistance. (b) Comparison of the current wave form between the simulations and the experimental data.

14 nC and then decreases to an asymptotic value  $\sim 10.5$  nC as the charged zone continues to expand. The maximum charge density of  $8 \mu\text{C}/\text{cm}^2$  shown in Fig. 12(a) corresponds to the electric field at the target surface  $\sim 100$  MV/cm. This charge density multiplied by the emission surface  $\sim \pi R_p^2 \sim 0.1 \text{ mm}^2$  gives the total charge of 10 nC. These values are also in good agreement with the model.

We computed also with the SOPHIE code the recharge electric current measured at the bottom of our target assembly. The simulation handles the target in a simplified geometry of the Eclipse chamber of the total volume  $1 \text{ m}^3$ . The grid size in that case is 1 mm. A connection of the target to the cable is simulated by a  $50\text{-}\Omega$  resistance between the stick and the pedestal, as shown in Fig. 13(a). As we cannot mesh the whole domain inside the chamber (more than 1 m) with a sufficient discretization of the space charge on the target, the recharge current was calculated with the SOPHIE code using the target charge evaluated during the electron emission phase shown in Fig. 12(b). The initial emission spectrum (the source term in Fig. 9) is filtered by the potential barrier (180-keV cutoff). The comparison of the calculated current wave form with the experimental results in Fig. 13(b) shows a very good agreement.

## V. CONCLUSIONS

A model of target polarization due to the hot-electron ejection from the laser irradiated spot is presented. The charge is accumulated as the electrons heated in laser plasma interaction are leaving the target. The ejection time varies from a few ps for the case of subpicosecond laser pulses to a few tens of ps for longer picosecond laser pulses. This time is defined by the cooling time of hot electrons in Coulomb collisions with the target electrons and ions. Therefore, the accumulated charge depends on the target material, and it decreases as the target density increases. The effective size of the charged zone is much larger than the laser focal spot. It is a few times larger than the hot-electron mean free path in the target. Therefore, the targets with a size smaller than  $\langle R_s \rangle$  accumulate smaller charge, while it is independent of the size for larger targets. The accumulated charge depends strongly on the hot-electron energy and thus on the laser intensity.

The target charge is measured experimentally by measuring the discharge current through the coaxial cable connecting the target to the ground. The duration of the discharge current is of the order of a few ns. It is defined by the impedance of the target assembly and the target support. It is much longer than the charging time, which does not exceed a few ps for our experimental conditions. That fact confirms the major hypothesis of the model, which neglects the discharge current from the target support. The observed dependence of the accumulated charge on the laser pulse energy and duration can be explained qualitatively with the model and with the numerical simulations. However, some quantitative differences need further analysis.

The experiment has been modeled in a series of numerical simulations that describe the laser-target interaction and hot-electron production, the electron spreading in the target, and the electron propagation through the vacuum chamber

to the conducting boundaries. Although the overall size of the simulation box (about a few millimeters) is smaller than the real experimental chamber, the major quantitative characteristics of the charging process are successfully described. The hot electrons contain a significant part of the laser pulse energy (25–50% depending on the interaction conditions) and the dominant part has an almost isotropic energy distribution with the exponential energy distribution. The characteristic electron temperature for the chosen laser intensity agrees well with the ponderomotive and Beg's scaling laws. The electron ejection from the target continues for about 1–2 ps, which is much longer than the laser pulse duration. The duration of the electron emission is defined by the process of hot-electron cooling in the electron-electron collisions. The electron emission process is inhibited by the formation of a potential barrier (of a virtual cathode) that repels electrons and suppresses the emission process. The potential barrier amplitude is comparable to the hot-electron initial temperature.

The model of the target polarization successfully explains also the data from the experiments with the picosecond laser pulses with the energies of hundreds of joules. The model predictions for several other experiments with higher laser-pulse energies are presented in Table I. In the experiments with the Titan and Omega EP lasers at the energy level of a few hundred joules and a picosecond pulse duration, the estimated charge is of a few  $\mu\text{C}$ . These numbers are in a reasonable agreement with the measured data and the simulation results [5–7], however, as the Omega EP pulse duration is rather long, our hypothesis of a steep target density profile might not be appropriate. Nevertheless, a comparison with the available measurements shows that the model accounts for the major effects that define the target polarization in high-intensity laser-plasma experiments. It provides us with an estimate for the polarization effect in the future experiments with the Petal laser system [35], which will deliver a power of 2 PW at the intensity of  $\sim 10^{20} \text{ W}/\text{cm}^2$ . It is expected that in the interaction with a copper target the charge could be about 20  $\mu\text{C}$ , and the hot electrons may spread over a few cm from the laser spot. The charging time of 200 ps is already comparable with the discharge time. This time can be exaggerated in our simple model, which does not account for collective energy losses of hot electrons. That effect can be significant at high laser pulse intensities if the hot-electron current density exceeds  $10^{12} \text{ A}/\text{cm}^2$  [36].

The model of charge polarization suggests methods of control of the charging process by choosing the target material, the size, and the support. The charging process also sheds the light on the emission of electromagnetic signal from the target. Two distinct sources of electromagnetic emission can be readily identified. The first one is related to the charging process. The electromagnetic pulse is emitted by the bunch of electrons ejected from the target. The electron bunch duration of a few ps corresponds to the frequency range of the order of a THz or a few tenths of a THz. The second pulse of a ns duration and in the frequency range below a few GHz is due to the discharge current through the target support. The detailed characteristics of this second electromagnetic pulse depend on the target and chamber geometry.

TABLE I. Thick target polarization characteristics for several sets of experimental parameters. The laser-to-electron conversion efficiency is 40%,  $c_0 = 1.0$ .

Parameter	Facility					
	Eclipse 1	Eclipse 2	Eclipse 3	Titan	Omega EP	Petal
Wavelength, $\lambda_{\text{las}}$ , $\mu\text{m}$	0.8	0.8	0.8	1.05	1.05	1.05
Pulse duration FWHM, $t_{\text{las}}$ , ps	0.05	0.40	0.05	2.0	9.0	0.5
Pulse energy, $\mathcal{E}_{\text{las}}$ , J	0.1	0.1	0.03	200	950	1000
Focal spot FWHM, $\mu\text{m}$	7.5	7.5	7.5	20	25	50
Laser int., $I_{\text{las}}$ , $10^{18}$ W/cm <sup>2</sup>	2.95	0.37	0.88	20.7	14	66
Laser amplitude, $a_0$	1.17	0.41	0.64	4.1	3.3	7.3
Target material	Copper	Copper	Copper	Aluminum	Tantalum	Copper
Electron temperature $T_{h0}$ , keV	276	133	179	1630	1280	3250
Maximum potential $ \Phi_{\text{min}} $ , kV	1650	820	1000	9800	8800	20000
Total charge of electrons, $Q_{\text{tot}}$	68 nC	159 nC	34 nC	18 $\mu\text{C}$	110 $\mu\text{C}$	43 $\mu\text{C}$
Cooling time, $t_{\text{cool}}$ , ps	1.07	0.38	0.57	62	9.6	84
e-i collision time, $t_{ei}$ , ps	0.58	0.19	0.29	57	4.2	59
Radius of electron dist. $R_p$ , mm	0.30	0.08	0.13	30	3.1	37
Target charge–model, $Q$	15.7 nC	3.9 nC	5.2 nC	6.0 $\mu\text{C}$	3.7 $\mu\text{C}$	21 $\mu\text{C}$
Target charge–simulation, $Q$	10.0 nC				1.2 $\mu\text{C}$	
Max. current, $J_h$ , kA	16	6.1	8.5	120	170	300

### ACKNOWLEDGMENTS

This work is partly supported by the EURATOM within the ‘‘Keep-in-Touch’’ activities and the Aquitaine Regional Council. We acknowledge the financial support from the French National Research Agency (ANR) in the frame of ‘‘the Investments for the future’’ Programme IdEx Bordeaux-LAPHIA (ANR-10-IDEX-03-02).

### APPENDIX: ONE-DIMENSIONAL MODEL OF THE ELECTRON DEBYE SHEATH

Following Ref. [18], we consider a semi-infinite stationary plasma with cold ions having a steplike density profile,

$$n_i(x) = \begin{cases} n_0 & \text{if } x < 0, \\ 0 & \text{if } x > 0. \end{cases} \quad (\text{A1})$$

The electrons having the temperature  $T$  are distributed near the plasma boundary according to the Boltzmann law,  $n_e = n_0 \exp(e\Phi/T)$ , in the self-consistent electrostatic potential  $\Phi$ . The latter is defined by the Poisson equation

$$\epsilon_0 \frac{d^2\Phi}{dx^2} = en_0 \begin{cases} \exp(e\Phi/T) - 1 & \text{if } x < 0, \\ \exp(e\Phi/T) & \text{if } x > 0. \end{cases} \quad (\text{A2})$$

It has to be solved with the asymptotic condition  $\Phi \rightarrow 0$  at  $x \rightarrow -\infty$ , corresponding to the plasma neutrality far from the boundary, and  $d\Phi/dx \rightarrow 0$  at  $x \rightarrow \infty$ , corresponding to the zero electric field far from the plasma and requiring the continuity of the potential and its first derivative at the boundary  $x = 0$ .

It is convenient to introduce the dimensionless potential  $\phi = e\Phi/T$  and to normalize the coordinate  $x = \xi\lambda_D$  by the Debye length  $\lambda_D = (\epsilon_0 T/e^2 n_0)^{1/2}$ . Then the first integral of the Poisson equation (A2) outside the plasma reads  $(\phi')^2 = 2e^\phi$ .

The choice of the integration constant corresponds to the fact that  $\phi$  and  $\phi'$  are negative, and  $\phi$  diverges at infinity,  $\phi \rightarrow \infty$  at  $x \rightarrow \infty$ . Integrating once more this equation, we find the potential outside the plasma,

$$\phi(x > 0) = -2 \ln(b_0 + \xi/\sqrt{2}). \quad (\text{A3})$$

The integration constant  $b_0$  will be defined from the potential continuity at the boundary.

The first integral of the Poisson equation (A2) inside the plasma reads  $(\phi')^2 = 2(e^\phi - \phi - 1)$ . The choice of the constant corresponds to the boundary condition at  $x \rightarrow -\infty$ . Equating the potential derivatives at the boundary for the inner and outer solutions, we find readily the value of the potential,  $\phi(0) = -1$ , and then the value of the integration constant  $b_0 = \sqrt{e}$  follows from Eq. (A3).

In the dimensional units the expressions for the electric potential and plasma density outside the plasma,  $x > 0$ , read as follows:

$$\begin{aligned} e\Phi(x > 0) &= -2T \ln(\sqrt{e} + x/\lambda_D \sqrt{2}), \\ n_e &= n_0 (\sqrt{e} + x/\lambda_D \sqrt{2})^{-2}. \end{aligned} \quad (\text{A4})$$

One can obtain also the expression for the electric field at the boundary  $E_s = (2/e)^{1/2} T/e\lambda_D$ , which corresponds to the charge surface density  $\sigma_s = \epsilon_0 E_s = (2\epsilon_0 n_0 T/e)^{1/2}$ .

The electron density distribution at the plasma surface has been calculated in the paper by Crow *et al.* [18] and Carron and Longmire [19]. However, Carron and Longmire did not account for the field penetration inside the plasma. Therefore, their solution with  $b_0 = 1$  does not account for the plasma charge neutrality.

- [1] A. G. MacPhee, K. U. Akli, F. N. Beg, C. D. Chen, H. Chen, R. Clarke, D. S. Hey, R. R. Freeman, A. J. Kemp, M. H. Key, J. A. King, S. Le Pape, A. Link, T. Y. Ma, H. Nakamura, D. T. Offermann, V. M. Ovchinnikov, P. K. Patel, T. W. Phillips, R. B. Stephens, R. Town, Y. Y. Tsui, M. S. Wei, L. D. Van Woerkom, and A. J. Mackinnon, *Rev. Sci. Instrum.* **79**, 10F302 (2008).
- [2] S. J. Gitomer, R. D. Jones, F. Begay, A. W. Ehler, J. F. Kephart, and R. Kristal, *Phys. Fluids* **29**, 2679 (1986).
- [3] A. Macchi, M. Borghesi, and M. Passoni, *Rev. Mod. Phys.* **85**, 751 (2013).
- [4] P. Gibbon, *Short Pulse Laser Interactions with Matter* (Imperial College Press, London 2005).
- [5] M. J. Mead, D. Neely, J. Gauvain, R. Heathcote, and P. Patel, *Rev. Sci. Instrum.* **75**, 4225 (2004).
- [6] C. G. Brown Jr., A. Throop, D. Eder, and J. Kimbrough, *J. Phys. Conf. Ser.* **112**, 032025 (2008).
- [7] D. C. Eder, A. Throop, C. G. Brown Jr., J. Kimbrough, M. L. Stowell, D. A. White, P. Song, N. Back, A. MacPhee, H. Chen, W. DeHope, Y. Ping, B. Maddox, J. Lister, G. Pratt, T. Ma, Y. Tsui, M. Perkins, D. O'Brien, and P. Patel, Lawrence Livermore National Laboratory Report LLNL-TR-411183 (2009).
- [8] F. S. Felber, *Appl. Phys. Lett.* **86**, 252501 (2005).
- [9] Chen *et al.*, *Phys. Plasmas* **19**, 113116 (2012).
- [10] C. G. Brown Jr., E. Bond, T. Clancy, S. Dangi, D. Eder, W. Ferguson, J. Kimbrough, and A. Throop, *J. Phys. Conf. Ser.* **244**, 032001 (2010).
- [11] F. N. Beg, A. R. Bell, A. E. Dangor, C. N. Danson, A. P. Fews, M. E. Glinsky, B. A. Hammel, P. Lee, P. A. Norreys, and M. Tatarakis, *Phys. Plasmas* **4**, 447 (1997).
- [12] M. G. Haines, M. S. Wei, F. N. Beg, and R. B. Stephens, *Phys. Rev. Lett.* **102**, 045008 (2009).
- [13] R. P. J. Town, C. Chen, L. A. Cottrill, M. H. Key, W. L. Kruer, A. B. Langdon, B. F. Lasinski, R. A. Snavely, C. H. Still, M. Tabak, D. R. Welch, and S. C. Wilks, *Nucl. Instrum. & Methods A* **544**, 61 (2005).
- [14] J. D. Jackson, *Classical Electrodynamics* (Wiley, New York, 1975).
- [15] K. Kanaya and S. Okayama, *J. Phys. D: Appl. Phys.* **5**, 43 (1972).
- [16] H. Chen, R. Shepherd, H. K. Chung, A. Kemp, S. B. Hansen, S. C. Wilks, Y. Ping, K. Widmann, K. B. Fournier, G. Dyer, A. Faenov, T. Pikuz, and P. Beiersdorfer, *Phys. Rev. E* **76**, 056402 (2007).
- [17] V. M. Ovchinnikov, G. E. Kemp, D. W. Schumacher, R. R. Freeman, and L. D. Van Woerkom, *Phys. Plasmas* **18**, 072704 (2011).
- [18] J. E. Crow, P. L. Auer, and J. E. Allen, *J. Plasma Phys.* **14**, 65 (1975).
- [19] N. J. Carron and C. L. Longmire, *IEEE Trans. Nucl. Sci.* **23**, 1986 (1976).
- [20] M. Passoni, V. T. Tikhonchuk, M. Lontano, and V. Yu. Bychenkov, *Phys. Rev. E* **69**, 026411 (2004).
- [21] J. Myatt, W. Theobald, J. A. Delettrez, C. Stoeckl, M. Storm, T. C. Sangster, A. V. Maximov, and R. W. Short, *Phys. Plasmas* **14**, 056301 (2007).
- [22] S. Jacquemot and A. Decoster, *Laser Part. Beams* **9**, 517 (1991).
- [23] C. Courtois, A. Compant La Fontaine, O. Landoas, G. Lidove, V. Méot, P. Morel, R. Nuter, E. Lefebvre, A. Boscheron, J. Grenier, M. M. Aléonard, M. Gerbaux, F. Gobet, F. Hannachi, G. Malka, J. N. Scheurer, and M. Tarisien, *Phys. Plasmas* **16**, 013105 (2009).
- [24] E. Lefebvre, N. Cochet, S. Fritzier, V. Malka, M. M. Aléonard, J. F. Chemin, S. Darbon, L. Disdier, J. Faure, A. Fedotoff, O. Landoas, G. Malka, V. Méot, P. Morel, M. Rabec Le Gloahec, A. Rouyer, Ch. Rubbelynck, V. Tikhonchuk, R. Wrobel, P. Audebert, and C. Rousseaux, *Nucl. Fusion* **43**, 629 (2003).
- [25] A. Compant La Fontaine, C. Courtois, and E. Lefebvre, *Phys. Plasmas* **19**, 023104 (2012).
- [26] M. L. Fensin, J. S. Hendricks, and S. Anghaie, *J. Nucl. Sci. Technol.* **170**, 68 (2010).
- [27] O. Cessenat, [arXiv:1301.4539](https://arxiv.org/abs/1301.4539); CHOCS - Revue scientifique et technique de la Direction des applications militaires, N 44, p. 25 (2013).
- [28] A. Pukhov, *Rep. Prog. Phys.* **66**, 47 (2003).
- [29] M. I. K. Santala, E. Clark, I. Watts, F. N. Beg, M. Tatarakis, M. Zepf, K. Krushelnick, A. E. Dangor, T. McCanny, I. Spencer, R. P. Singhal, K. W. D. Ledingham, S. C. Wilks, A. C. Machacek, J. S. Wark, R. Allott, R. J. Clarke, and P. A. Norreys, *Phys. Rev. Lett.* **84**, 1459 (2000).
- [30] W. L. Kruer and K. Estabrook, *Phys. Fluids* **28**, 430 (1985).
- [31] G. Malka and J. L. Miquel, *Phys. Rev. Lett.* **77**, 75 (1996).
- [32] S. C. Wilks, W. L. Kruer, M. Tabak, and A. B. Langdon, *Phys. Rev. Lett.* **69**, 1383 (1992).
- [33] A. Pukhov and J. Meyer-ter-Vehn, *Phys. Plasmas* **5**, 1880 (1998).
- [34] G. Liu and S. Gedney, *Microwave Opt. Technol. Lett.* **25**, 8 (2000).
- [35] <http://petal.aquitaine.fr/>
- [36] B. Vauzour, J. J. Santos, A. Debayle, S. Hulin, H.-P. Schlenvoigt, X. Vaisseau, D. Batani, S. D. Baton, J. J. Honrubia, Ph. Nicolai, F. N. Beg, R. Benocci, S. Chawla, M. Coury, F. Dorchie, C. Fourment, E. d'Humières, L. C. Jarrot, P. McKenna, Y. J. Rhee, V. T. Tikhonchuk, L. Volpe, and V. Yahia, *Phys. Rev. Lett.* **109**, 255002 (2012).